ELSEVIER

Polymer 42 (2001) 1621–1631

polymer

www.elsevier.nl/locate/polymer

Secondary structure and elevated temperature crystallite morphology of nylon-6/layered silicate nanocomposites

D.M. Lincoln[a], R.A. Vaia[a,*], Z.-G. Wang[b], B.S. Hsiao[b]

[a]*Air Force Research Laboratory, Materials and Manufacturing Directorate, Wright-Patterson AFB, Dayton, OH 45433, USA*
[b]*Department of Chemistry, State University of New York at Stony Brook, Stony Brook, NY 11794-3400, USA*

Received 29 March 2000; received in revised form 25 May 2000; accepted 25 May 2000

Abstract

Mesoscale (secondary) structure arising from association of layered silicates is quantified and its impact, along with constituent interactions, on elevated temperature crystallite morphology in nylon-6/montmorillonite nanocomposites is examined. Simultaneous small- and wide-angle X-ray scattering and diffraction methods are developed to provide detailed information on the secondary structure of the layered silicate and the structure of the crystalline polymer in the presence of the layered silicate. Ultra-long range order (20–60 nm) of the inorganic layers is observed at low-volume fractions (0.8 vol%). Elevated temperature (205°C) crystallite morphology of the nylon-6 matrix depends on the secondary structure and interfacial interactions. Smaller, more disordered lamellae are observed in the in situ polymerized nanocomposites whereas larger, more ordered lamellae are observed in melt-processed nanocomposites.

Keywords: Nylon-6/layered silicate nanocomposites; Mesoscale structure; Crystallite morphology

1. Introduction

Nanoscale polymer–inorganic composites have been the focus of intense research over the past decade. The interest stems not only from their use in practical applications, such as sporting equipment and under-the-hood automobile components, but also from the fundamental issues relative to the nanoscale constraints on the polymer and the ultra-large specific interfacial area between the constituents. Polymer-layered silicate nanocomposites (PLSN) are representative of these materials, consisting of 1 nm thick aluminosilicate layers dispersed in a polymer matrix. PLSN, such as nylon–montmorillonite nanocomposites, exhibit superior properties when compared to the pure counterparts [1–9]. Most notable are the unexpected properties obtained from the addition of a stiff filler to a polymer matrix, like the retention of the impact strength [1,2], increased atomic oxygen resistance [7], and improved ablative performance [8]. Along with the unexpected properties come the more predictable enhancements such as increased modulus [1,3], increased gas barrier [4,5], increased heat distortion temperature (HDT) [1,3], and resistance to small molecule permeation [6]. These enhancements occur with only 1–4 vol% addition of high aspect ratio filler, which leads to reduced price in terms of filler concentration [8,9] and retention of polymeric processability.

The majority of recent work on PLSN has focused on synthesis and characterization of physical properties [9–16]. However, the fundamental mechanisms for property enhancements in these 'exfoliated' PLSN, whether rigid-particulate reinforcement (e.g. interparticle connectivity and percolation) or alteration of equilibrium chain conformations near the polymer–inorganic interface, are not fully understood. Establishment of these structure–property relationships is complicated by a significant number of morphological and processing factors that impact both the inorganic filler and polymer, such as heterogeneity of the nanoscale arrangement, orientational distribution of the layers, strength of polymer–inorganic interactions and the influence of inorganic arrangement on polymer conformation and morphology.

For semicrystalline polymers, the nanoscopic arrangement of crystal lamellae is comparable to the distribution of inorganic fillers and can lead to an interesting confluence of two nanoscale morphological features. Previous studies of polyamide/montmorillonite nanocomposites revealed that the global orientation of the silicate layers, arising from flow alignment, dictates the orientation of the crystal phase. Wide-angle X-ray diffraction experiments have

* Corresponding author. Tel.: +1-937-255-9184; fax: +1-937-255-9157.
E-mail address: richard.vaia@afrl.af.mil (R.A. Vaia).

0032-3861/01/$ - see front matter
PII: S0032-3861(00)00414-6

indicated that the chain axes are normal to the silicate layers in the interior of an injection molded components, while they are parallel to the layers in the near surface region of molded and extruded components [17]. In addition, the formation of a different crystalline phase [18,19] and the possible presence of a higher melting temperature phase have also been reported [18]. The more ductile γ-phase [20] that is formed may contribute greatly to the observed changes in properties of the material, specifically the toughness. Evidence has also been found that the layers affect not only the formation of the lamellae but also the spherulites [21], which may also be a root of some of the property enhancements.

In addition to the confinement of crystallization to nanoscopic dimensions, a large fraction (>30% [11]) of the polyamide chains are purported to be end-tethered to the silicate surface through ionic interactions. The areal density of ionic interactions (1.7–2.0 chains/nm [2]) implies these tethered chains are in the extended brush regime [22,23]. Related investigations of diblock copolymers and blends have also found that the density of brushes in the extended brush regime can have an effect on the morphology near the interface [24,25]. In polyamide/polysulfone systems it is reported that a higher density of polyamide brushes attached to polysulfone surfaces resulted in lower ordering of the lamellar stacking and crystal lattice [25]. In general, a detailed understanding of the effects of constituent interactions and nanoscale confinement on polymer crystallization and subsequent structure and lamella arrangement is not yet well understood.

The objective of our efforts is to investigate the influence of nano (primary) and mesoscale (secondary) structure in PLSNs and of interfacial interactions between constituents on the morphology development of a semicrystalline polymer matrix, such as nylon-6. In this first part of a series, simultaneous small- and wide-angle X-ray scattering and diffraction methods are developed to provide detailed information on the secondary structure of the layered silicate and the structure of the crystalline polymer in the presence of the layered silicate. Specifically, the influence of silicate layer concentration and interfacial interactions (in situ polymerized PLSN with interface containing end-grafted polymer chains; melt-processed PLSN with interface dominated by secondary interactions) on the secondary structure of the layered silicate and the elevated temperature crystallite morphology of nylon-6 (205°C) is examined. Subsequent parts will discuss isothermal and nonisothermal crystallization behavior of these semicrystalline PLSNs.

2. Experimental

2.1. Materials

Commercially available 5 wt% (NCH5) and 2 wt% (NCH2) layered silicate/nylon-6 in situ polymerized nanocomposite materials and pure nylon-6 polymer (Nyl6) were obtained from Ube Industries, Ltd. (Japan). The in situ polymerization has been detailed elsewhere [11]. In summary, organically modified montmorillonite was prepared by a cation exchange reaction with 12-aminolauric acid. Subsequent ring-opening polymerization of ϵ-caprolactam initiated by the pendant carboxylic acids on the surface of the modified montmorillonite reportedly results in approximately 50% (NCH5) and 30% (NCH2) of the nylon-6 chains 'tethered' to the surface of the montmorillonite via ionic interaction of the primary ammonium cation [11]. The resultant molecular weights (g/mol) of the nylon-6 polymer in PLSN are 22,200 (NCH2) and 19,700 (NCH5), respectively [26].

In addition to the in situ polymerized nylon-6 nanocomposite, melt-processed nylon-6 nanocomposite was also examined. A 4 wt% montmorillonite/nylon-6 nanocomposite (thermal decomposition experiments revealed an organoclay content of ~3.7 wt% [8]) (NLS4) was obtained from Southern Clay Products, Inc. (Gonzalez, Texas). The melt-processed material was produced by blending Cloisite 30A (organically modified montmorillonite, Southern Clay Products, Inc.) and nylon-6 (Capron 8209, Allied Signal Co.) using a twin-screw extruder with a zone-1 temperature of 240°C, zone-2 temperature of 220°C and die temperature of 245°C operating at 180 rpm. In contrast to the in situ polymerized material, weak secondary interactions, such as van der Waals interactions, dominate the polymer–silicate interactions in the melt-processed NLS4, resulting in drastically different polymer–silicate nanoscopic and interfacial morphologies.

The PLSN were obtained in pellet form and dried under vacuum at 70–80°C for 3–4 h prior to compression molding into 7 mm circular disks approximately 1 mm thick for X-ray scattering experiments. Platens of a Carver hydraulic press were pre-heated to ~280°C. The mold containing approximately six pellets was placed between the platens and allowed to heat for several minutes before 500 lb of pressure was applied. The pressure was kept constant as the mold was heated gradually to ~230–240°C over approximately 12 min. Finally the mold was removed and allowed to cool before removing the samples. Quenched samples were made by heating the compression molded disks to 250°C for 5 min in a copper holder and then submersing in liquid nitrogen.

2.2. Transmission electron microscopy (TEM)

The TEM micrographs were collected as described previously [27]. The samples were embedded in the Spurr epoxy and cured at 80°C for 12 h. X-ray diffraction (XRD) of the post cured specimens revealed that curing did not alter the structure of the materials. The epoxy blocks were cut into triangular block faces (ca. 1×0.5 mm) for microtoming. Ultrathin sections (100 nm or less) were microtomed from these faces at room temperature using a

Reichert ultramicrotome. A water-filled boat, attached to the diamond knife, served to float the ultrathin sections after microtoming. The sections were then collected on gold TEM grids (hexagonal 400 mesh) and dried completely on filter paper.

TEM investigations were performed using a Phillips CM200 TEM with a LaB_6 filament operating at 200 kV. Extra precautions were taken to minimize sample motion and beam damage of the samples. The TEM grids were mounted in a liquid nitrogen cooled sample holder and the brightness of the electron beam was minimized (low-dose mode). Despite the precautions taken here the contrast of the area under investigation began to fade after a few minutes of beam exposure. The fading is attributed to destruction of the structure of the silicate layers and possible expulsion of interlayer organics by the electron beam [28–31]. All images were collected before contrast loss became visibly noticeable.

2.3. X-ray characterization

Simultaneous small-angle (SAXS) and wide-angle (WAXS) X-ray scattering experiments were conducted at the Advanced Polymers Beamline (X27C) of the National Synchrotron Light Source (NSLS), Brookhaven National Laboratory (BNL). The wavelength of the incident X-rays was 1.307 Å, defined by a double multi-layer monochromator. The synchrotron X-rays were collimated to a 600 μm beam size using a three pinhole collimator [32]. Data were collected using two Braun linear position sensitive detectors [33] at 190 (SAXS) and 20 cm (WAXS). The scattering angle was calibrated using silver behenate (SAXS) and quartz (WAXS). Elevated temperature and isothermal crystallization measurements were carried out using a dual oven temperature-jump apparatus [32]. Samples, mounted in copper holders, were initially melted at 250°C for 5–8 min and shuttled to the second oven aligned in the X-ray beam set at the desired temperatures ($T = 250$ or 205°C) for measurement. Data acquisition times were 0.25–4 min per scan. All the X-ray data were corrected for beam fluctuations and sample absorption.

3. Data analysis

3.1. Small-angle X-ray scattering

Nominally, the SAXS data contain contributions from both the crystalline polymer as well as the dispersed silicate layers. Detailed analysis of the scattering associated with the crystalline polymer regions required careful removal of the layered silicate scattering. This is accomplished by a point-by-point subtraction of the scattering pattern collected at $T > T_m$ (melt temperature) from the pattern collected at $T = T_{iso}$ (isothermal crystallization temperature). To eliminate potential heterogeneity associated with processing, the scattering patterns were collected consecutively from the sample without disturbing the sample position or apparatus. At $T > T_m$ the layers are dispersed in a uniform, amorphous background consisting of molten polymer. Assuming the crystallization process does not substantially alter the distribution of layers, the SAXS profile of the molten PLSN may be used to remove the contributions of the layers at $T = T_{iso}$. Re-melting a crystallized sample verified that the scattering, and thus morphology, from the inorganic layers did not change during the crystallization process. However, note that these experiments do not unequivocally demonstrate that, in the general case, layer distribution is insensitive to the crystallization process. Additionally the scattering density $\Delta\rho$ of the polymer medium relative to the silicate changes only minimally upon formation of 10–30 vol% crystallites ($\Delta\rho_{melt} = 3.16 \times 10^{23}$ e$^-$/cm^3; $\Delta\rho_{crystal} = 3.86 \times 10^{23}$ e$^-$/cm^3).

Small-angle X-ray scattering data from the crystalline portion can then be analyzed by correlation and interface distribution methods [34]. Detailed descriptions and examples may be found in the literature and thus will only be briefly described here. It should be noted that the correlation function method is general, the specific parameters extracted from the analysis are with respect to an assumed morphological model. For the PLSN case, the finite lamellar stacks model is assumed since each of the scattering entities (silicate layers and crystal lamellae) in the system can be considered plate-like.

The scattering intensity $I(q)$ measured from an isotropic distribution of lamellar objects can be transferred to a one-dimensional intensity $I_1(q)$ by Lorentz correction [35]

$$I_1(q) = cI(q)q^2 \tag{1}$$

where c is a constant. In this case, SAXS data can be analyzed via a combination of the one-dimensional correlation $\gamma_1(r)$ and the interface distribution function $g_1(r)$ as the following [36–39].

$$\gamma_1(r) = \int_0^\infty I_1(q)\cos(qr)\,\mathrm{d}q/Q \tag{2}$$

$$g_1(r) = \mathrm{d}^2[\gamma(r)]/\mathrm{d}r^2 = -\int_0^\infty I_1(q)q^2\cos(qr)\,\mathrm{d}q/Q \tag{3}$$

where q is the scattering vector ($q = [2\pi/\lambda]\sin(2\theta)$ and 2θ is the scattering angle) and Q is the invariant defined as

$$Q = \int_0^\infty I_1(q)\,\mathrm{d}q \tag{4}$$

For the pinhole geometry, the correlation function for a random distribution of plate-like particles is the Fourier transform of the Lorentz corrected SAXS profile [36], while the interface distribution function $g_1(r)$ is the Fourier transform of the interference function $G_1(q)$ [38,39].

$$g_1(r) = \int_0^\infty G_1(q)\cos(qr)\,\mathrm{d}q \tag{5}$$

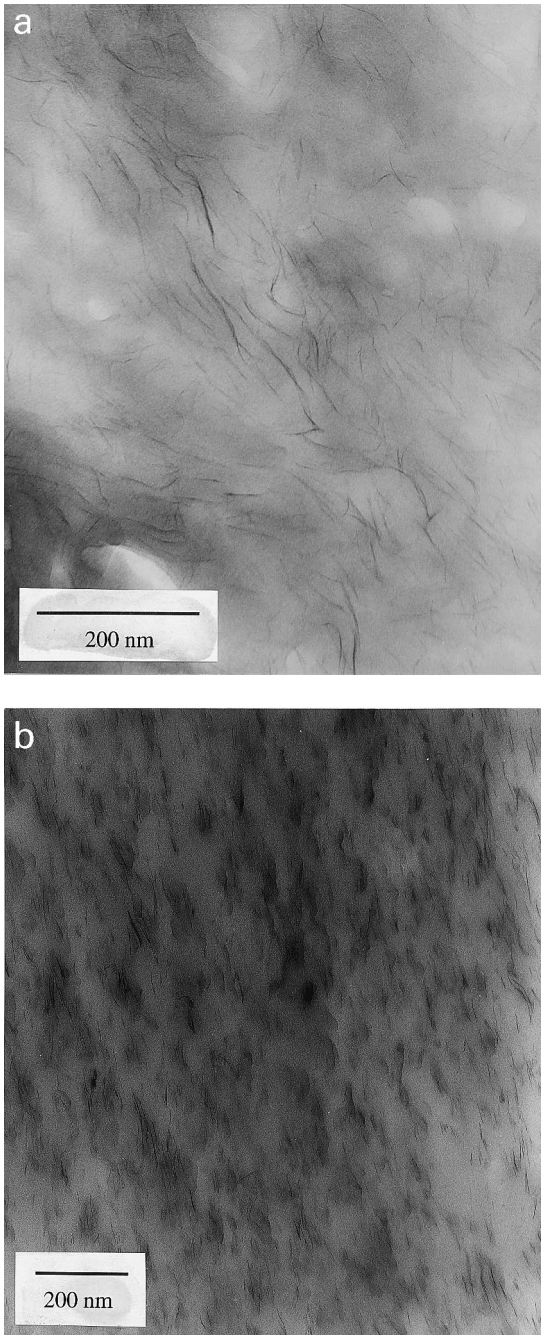

Fig. 1. Bright field transmission electron micrographs of (a) in situ polymerized NCH5 nanocomposite (b) melt-processed NLS4 nanocomposite.

where $G_1(q)$ can be expressed as

$$G_1(q) = \lim_{q\to\infty} I_1(q)q^2 - I_1(q)q^2 \tag{6}$$

For the above relations, integration is to be carried out over the range of $0 \le q \le \infty$. Since SAXS data are collected in a finite angular range ($q_{min} = 0.06\ nm^{-1} < q < q_{max} = 3.0\ nm^{-1}$, in this case), it is necessary to extrapolate the scattering intensity to both low and high q values before Fourier transformation. Correct extrapolation is critical to final results. The extrapolation to low q uses the general method as described previously [40]. The extrapolation to high q was performed with the aid of the Porod law, which is illustrated as follows.

At high q the measured scattering intensity $I_{obs}(q)$ includes the contributions from liquid-like 'background' scattering $I_b(q)$ and the finite interface between the two constituting phases. A Porod analysis is used to remove these contributions. The Porod law for this intensity can be expressed as [41]

$$\lim_{q\to\infty} I_{obs}(q) = I_b(q) + (K/q^4)\exp(-\sigma^2 q^2) \tag{7}$$

where σ is related to the width of the interface and K is the Porod constant. Instead of using the conventional method such as $I_{obs}q$ [4] versus q [4] to estimate the contributions of I_b and the exponential term [36,42], the following two criteria in the form of interference function can be used to satisfy the Porod law [40].

$$\lim_{q\to\infty} G_1(q) = \lim_{q\to\infty} \{K - [I_{obs}(q) - I_b(q)]q^4 \exp(\sigma^2 q^2)\}dq = 0 \tag{8}$$

$$\int_0^\infty G_1(q)dq = \int_0^\infty \{K - [I_{obs}(q) - I_b(q)]q^4 \exp(\sigma^2 q^2)\}dq = 0 \tag{9}$$

The second criterion is based on an assumption that if the presence of a finite transition zone between the two constituting phases (amorphous and crystalline polymer) has been accounted for, then the interface distribution function will start from the origin ($g_1(0) = 0$). Since $g_1(r)$ is the Fourier transform of $G_1(q)$, the total area of $G_1(q)$ versus q will be zero. Once the Porod constant K, the liquid scattering profile I_b, and the interface correction term σ have been estimated, the correlation and interface distribution functions can be easily calculated from the experimental data.

Structural details of the crystal lamellar stack can be derived from the correlation function. Herein the finite lamellar stacks model is assumed, comprised of a finite stack of lamellae separated by inter-lamellar regions of different scattering density. The long spacing can be estimated as the position of the first maximum in the correlation function. The two-phase analysis of the correlation function yields estimates for the average thickness of both regions (l_1 and l_2, or crystal and amorphous layer thickness) [34,43].

3.2. Wide-angle X-ray scattering

In the molten nylon-6-layered silicate nanocomposite, WAXS intensity is dominated by the amorphous molten polymer, since the magnitude of single layer form factor of the exfoliated silicates is negligibly small at q greater than the inverse of layer thickness.

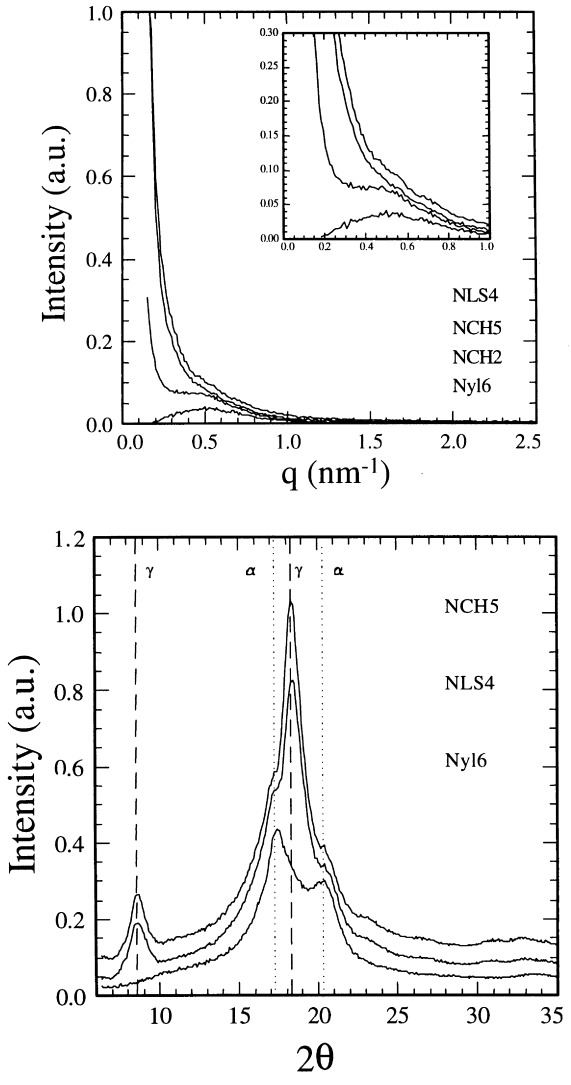

Fig. 2. SAXS and WAXS profiles of the quenched nylon-6 and nylon-6 nanocomposites. The curves are vertically offset for clarity.

Upon crystallization, the WAXS signal contains a superposition of crystalline peaks and a broad amorphous halo. Deconvolution of the pattern using the program GRAMS/32 Spectral Notebase™ (Galactic Industries Corporation) with Gaussian peak shape yields the integrated intensities, peak positions, peak heights and peak widths of respective crystal reflections and amorphous background. In this study, one Gaussian peak was used to describe the amorphous phase. The apparent degree of crystallinity, ϕ_{mc}, is proportional to the ratio of the total intensity of crystalline reflections to the total observed intensity (crystalline + amorphous). The calculated value of ϕ_{mc} is lower than the room-temperature value due to distortions in the crystal lattice and thermal disorder associated with the elevated temperatures examined.

4. Results

The results will be discussed in three parts: (1) morphological characterization of quenched PLSN; (2) detailed characterization of the secondary structure of the layered silicate; and (3) detailed characterization of the elevated temperature (205°C) crystalline morphology of the nylon-6 matrix.

4.1. Quenched nanocomposite

Bright field TEM micrographs of the quenched NCH5 and NLS4 samples are shown in Fig. 1. The dark lines are the montmorillonite layers perpendicular to the sample surface (~1 nm thick). The average diameters of the layers in NCH5 (160 ± 30 nm) are approximately twice as large as those in NLS4 (70 ± 20 nm). In general the mean layer spacing is between 35 and 45 nm in NCH5 and 40 and 60 nm in NLS4. Quantification of layer distribution from the mircographs is hampered because the image is representative of only an exceedingly small portion of the sample as well as the projection of a finite thickness. For example, higher magnification micrographs of NLS4 indicate that layer distribution is not uniform — a small fraction of aggregates containing 2–3 layers is observable.

Simultaneously collected SAXS and WAXS profiles of the quenched samples along with the pure polymer are shown in Fig. 2. The peaks at $2\theta = 17.4$ and 20.5 in the Nyl6 WAXS profile indicate that the pure nylon-6 crystallized predominantly into the α crystalline phase; whereas, the peaks at $2\theta = 8.6$ and 18.2 for the NCH5 and NLS4 profiles indicate that the nanocomposite samples predominantly contain the γ phase. For pure nylon-6, the α crystalline phase is thermodynamically stable and consists of sheets of hydrogen bonded chains formed between antiparallel chains. The γ crystalline phase is metastable and consists of random hydrogen bonding between parallel chains [44]. Ito et al. observed that the mechanical properties of the phases, as well as the temperature dependence, are different for the two phases [22]. The α phase exhibits a higher modulus below T_g but a more rapid decrease above T_g than the γ phase. This implies that the γ phase has a higher heat distortion temperature. Thus, the relative fraction of these crystalline phases is expected to impact the mechanical properties of the PLSN.

With regard to secondary (mesostructure), the SAXS profile for Nyl6 shows the presence of lamellar crystallites with a periodic spacing of 9.95 nm. In contrast, the profiles for the nanocomposites show a change in the intensity of this reflection with increased concentration of dispersed layers indicating a disruption of the lamellar superstructure by spatial arrangement of the silicate. Optical microscopy indicates that the spherilitic texture of pure nylon-6 is disrupted by the presence of the dispersed silicate layers, producing an axialitic texture. Since the fracture behavior of semicrystalline polymers is intimately related to the

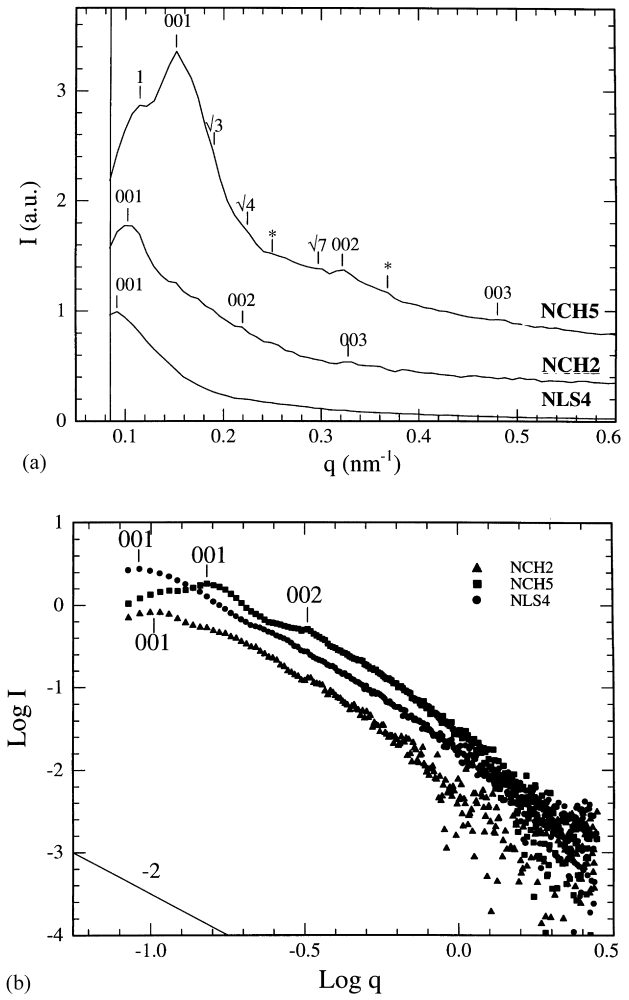

Fig. 3. Small-angle scattering data (a. I vs q; b. log(I) vs log(q)) at 250°C for NCH5, NCH2 and NLS4. Small-angle scattering data of neat nylon-6 at 250°C was commensurate to the background signal. Curves are vertically offset and the magnitudes are scaled by 0.54:1.17:1.00 for NLS4:NCH2:NCH5, respectively, for clarity.

spherulitic texture, the extent to which the lamella organization is altered should impact the mechanism of crack propagation and thus, fracture properties of these PLSNs.

4.2. Layered silicate

Quantification of the secondary structure associated with silicate layers is also possible using small-angle X-ray scattering (SAXS). Fig. 3 summarizes the small-angle scattering data at 250°C for NCH5, NCH2, and NLS4. Small-angle scattering data of neat nylon-6 at 250°C is commensurate to the background signal. Since 250°C is greater than the melting point of nylon-6 crystallites, the scattering is exclusively associated with the silicate layers that are dispersed in an isotropic polymer melt. The absence of strong basal reflections ($q \sim 2\ \mathrm{nm}^{-1}$, not shown) indicates a disruption of the original stacking of the silicate layers and is generally indicative of an exfoliated nanocomposite [27,45].[1] The absence of reflections associated with layer stacks observed in the TEM of NLS4 indicates that these stacks constitute a relatively minor fraction of the silicate phase (recall though, that the observed scattering arises from only 1–4 vol% of the sample and thus absolute sensitivity is limited).

Additional details are observable in the scattering pattern beyond the distribution of the original stacking of the silicate layers. In this region of reciprocal space, the montmorillonite layers can be adequately approximated as very thin plates (R, radius $\gg 2H$, thickness). The single particle scattering function of an isolated, thin plate is proportional to q^{-2} for $q < H^{-1}$ and exhibits a Guinier region around $qH = 1$ in which the q-dependence increases. Detailed discussion of scattering theory of plates and layered silicates is beyond the scope of this paper, but can be found in Refs. [46,47]. In the intermediate q-range ($0.4 < q < 2.0\ \mathrm{nm}^{-1}$), removed from the effects of interparticle correlations, the PLSN (Fig. 3b) exhibit q-dependence around -2.2, in agreement with finite plate-like scattering. Additionally, since the scattering regime is near $qH \sim 1$, analysis of the high q-data by the high-q-approximation to the form factor of a plate [48] indicates that the effective layer thickness for NCH5 and NLS4 is 2.7 ± 0.3 and 2.3 ± 0.4 nm, respectively. This is close to the thickness anticipated for a silicate layer (0.96 nm) coated with alkyl ammonium surfactants (0.7–0.9 nm).

Beyond plate-like scattering, Bragg reflections are observable. For NCH5, a prominent reflection at $q = 0.158\ \mathrm{nm}^{-1}$ and associated order reflections ($q = 0.322$ nm ($n = 2$); $q = 0.480\ \mathrm{nm}^{-1}$ ($n = 3$)) indicate a superstructure with a critical length of 39.8 nm exists. These results are consistent with the TEM micrographs. Theoretical estimation of mean layer–layer spacing for a uniform nematic-like arrangement of layers at 5 wt% (2.2 vol%) is approximately 45 nm, also in reasonable agreement with the observed reflections. Similarly for NCH2, a prominent reflection at $q = 0.105\ \mathrm{nm}^{-1}$ and associated order reflections ($q = 0.220$ nm ($n = 2$); $q = 0.320\ \mathrm{nm}^{-1}$ ($n = 3$)) indicate a superstructure with a critical length of 59.8 nm exists. Additionally, reflections very close to the beam stop for both NCH5 and NLS4 ($q = 0.114$ and $0.091\ \mathrm{nm}^{-1}$, respectively) persist after data correction, corresponding to potential structure at even larger distances (52.5 and 69.0 nm, respectively). Most surprising of all is the ability to index minor features in NCH5, with signal to noise a few times greater than background, to that anticipated for hexagonal packing of the layers. A higher level spatial correlation between

[1] Nominally, $1.85\ \mathrm{nm} < d_{001} < 2.50 (3.3\ \mathrm{nm}^{-1} > q > 2.5\ \mathrm{nm}^{-1})$ for organically modified montmorillonite and $3.0 < d_{001} < 3.5$ nm$(2.1 > q > 1.8\ \mathrm{nm}^{-1})$ for most intercalated polymer-organically modified silicate complexes.

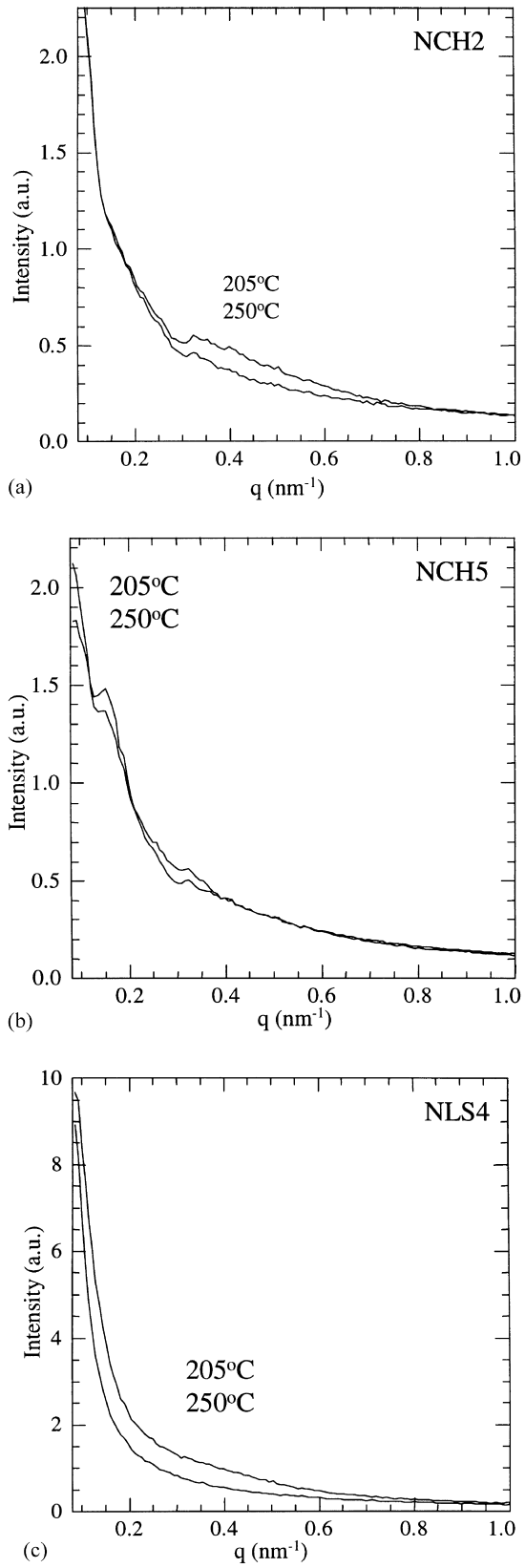

Fig. 4. SAXS data for the melt at 250°C and NCH2, NCH5 and NLS4 nanocomposites at 205°C. The NCH2, NCH5, and NLS4 samples have been isothermally crystallized for 65, 65, and 81 min, respectively.

layers was predicted by Balazs et al. at volume fractions between 5 and 40% [49–51]. Additional weak reflections, which are not easily indexed, are also apparent (Fig. 3a). Note that the observed structure is probably associated with processing history and cannot be unequivocally associated with a thermodynamically-stable discotic phase.

Finally, it is extremely important to note that the relative magnitude of the Bragg reflections and total scattered intensity (invariant) of the molten nanocomposite varied with sample processing history and even beam location (beam size ~300 μm) on the sample. For example, the invariant of NLS4 is twice as large as that for NCH5 even though there is less silicate in NLS4. These observations indicate micron or larger domains exist with varying concentration or orientation of the layers parallel to the sample surface (and perpendicular to the incident X-rays). Domains of different orientation may be separated by orientational defects such as observed in liquid crystal polymers and block copolymers. Preferred layer orientation in the pellets has been previously noted [52–54] and on the scale of individual pellets (1–5 mm) may not be substantially altered during compression molding. Furthermore, superposition of different layer organization in NCH5 indicates inhomogeneities in the initial concentration have not been equilibrated by processing. Determination of the translational and rotational diffusion rates of the layers is necessary to understand relaxation and homogenization of these structures in the melt.

Overall, these results indicate that silicate layers (primary structure) is only the initial level of morphological detail. A complex mesoscale arrangement of layers (secondary structure) exists and must be carefully characterized, especially since this structure is anticipated to be process history dependent.

4.3. Polymer crystallites

Normalized SAXS intensities at 205 and 250°C for (a) NCH2, (b) NCH5 and (c) NLS4 are shown in Fig. 4. Comparison of the melt profile (205°C) to that at 205°C reveals that the layered silicate scattering does not change upon crystallization as indicated by the similarity in the shape and retention of the Bragg peaks. Since the layered silicate contribution to the SAXS is unchanged, scattering from the elevated temperature (205°C) polymer crystallites is obtained from subtraction of the molten profile from the elevated temperature profile. Fig. 5 displays the excess scattering at 205°C from the various PLSNs. The correlation function method was used to extract the morphological parameters using a two-phase lamellae stacks model [40]. Fig. 6 shows the correlation functions for the crystalline polymer in the pure (Nyl6) and the nanocomposite (NCH2, NCH5, NLS4) samples. The resultant morphological parameters and constants are listed in Table 1. K and Q are the Porod constant and invariant, respectively. L_b is the Bragg d-spacing from the Lorentz corrected SAXS profile

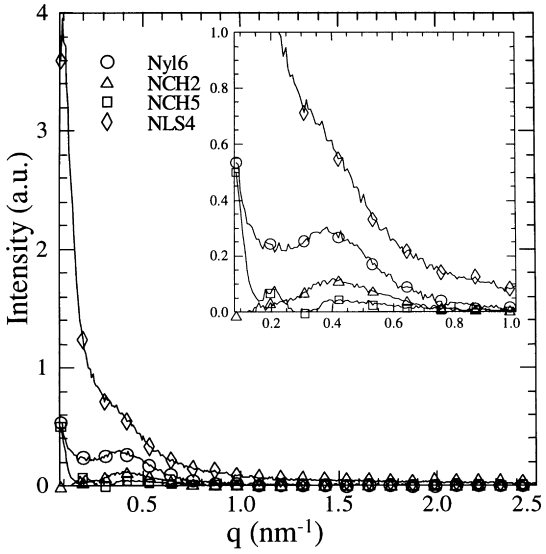

Fig. 5. SAXS profile at 205°C of nylon-6 compared to the excess scattering associated with the nylon-6 crystallites in the PLSNs.

and L_{cM} is the long period of the finite crystal lamellar stacks from the correlation function. Although the crystallinity in these samples is relatively low (<50%), we assume for discussion purposes that the larger value l_1 is the lamellar crystal thickness, l_c, and the smaller value l_2 is the amorphous layer thickness, l_a, based on previous assignments for PEEK [34], PBT [55], PET [56], and nylon-66 [57].

These results indicate that the fundamental structure of the polymer crystallite depends on silicate loading, morphology and interfacial interactions. The long period of nylon-6 decreases for the two nanocomposite samples in which a portion of the polymer chains are tethered to the surface (NCH2, NCH5) but increases when weak secondary interactions dominate at the interface (NLS4). Additionally, the invariant decreases for NCH2 and NCH5, consistent with increased disorder of the crystal lamella or within the lamella stack (decreased contrast, $\Delta\rho$).

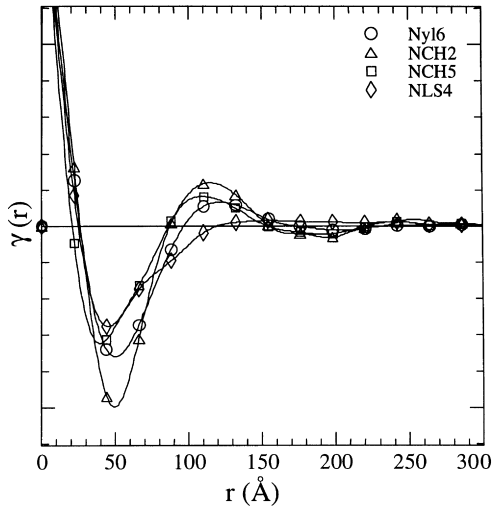

Fig. 6. Correlation plots for pure nylon-6 and excess scattering from the nylon-6 nanocomposites.

The WAXS profiles of the molten and isothermally crystallized samples are shown in Fig. 7. The peak positions of crystal reflections, amorphous background and the crystallinity were calculated by a deconvolution method, and results are summarized in Table 2.

The mean inter-chain spacings in the molten state are relatively unchanged upon addition of the montmorillonite layers. The presence of a 30–40 nm confinement by adjacent silicate layers does not compress the polymer (alter chain–chain spacing). This is consistent with related studies of free standing and supported polystyrene films, which have shown that density does not change down to a thickness of 0.4 Rg [58,59]. Upon isothermal crystallization at 205°C, the inter-chain spacings in the amorphous region decrease relative to the melt, and within experimental error, are independent of silicate loading. In contrast, the mean inter-chain spacing in the crystalline regions is smaller in Nyl6 than in the nanocomposites. Note that the WAXS profiles are markedly different than those of the quenched samples measured at room temperature since experimental temperature (205°C) in Fig. 7 is greater than the so-called Brill transition temperature [60,61].

5. Discussion

Secondary structure associated with long range ordering of the layered silicate (61 nm (NCH2), 41 nm (NCH5), and 68 nm (NLS4)) exist in nylon-6/montmorillonite nanocomposites. This mesoscopic arrangement of layers (40–60 nm) is on a comparable scale to typical polymer crystallites. As a result, it is anticipated that the morphology of the layered silicates (size, shape and distribution) will have a profound effect on the structure development and rate of crystallization of the semicrystalline polymer. Additionally, because of the nanoscale dimensions, the specific interactions between polymer chains and the silicate surface will influence chain mobility and thus the crystallization processes.

Initially, the WAXS profiles of the quenched samples reveal that addition of the montmorillonite layers causes a change in the crystal phase of nylon-6 from predominantly α to largely γ phase. Nylon-6 has also been shown to crystallize in the γ phase when iodized with an alcohol potassium iodide solution [62,63]. The supposition is that the iodine coordinates with the amide groups, forcing them out of the plane formed by the chains [64]. The proximity of the surface, irrespective of if the chains are ionically tethered (NCH5) or weakly bonded (NLS4), results in conformational changes of the chains, limiting the formation of H-bonded sheets leading to the appearance of the γ phase. Similar behavior has been observed in other filled polyamide systems [65]. Most surprising though is that even though the crystalline fraction of the quenched samples is comparable, the extent of lamellar organization (SAXS) is

Table 1
Morphological parameters at 205°C for nylon-6 in the pure (Nyl6) and nanocomposite (NCH2, NCH5, NLS4) samples isothermally crystallized at 205°C for 85, 65, 65, and 81 min, respectively

	l_1 (Å)	l_2 (Å)	L_b (Å)	L_{cM} (Å)	K (10^{-7})	Q (10^{-5})	Porod region
Nyl6	84.4	37.6	128.9	122.0	9.6	2.94	0.115 to 0.160
NCH2	79.3	38.7	123.2	118.0	1.4	1.08	0.105 to 0.135
NCH5	81.7	28.3	119.7	110.0	2.2	0.55	0.141 to 0.187
NLS4	124.7	31.3	137.3	156.0	25.3	7.37	0.112 to 0.162

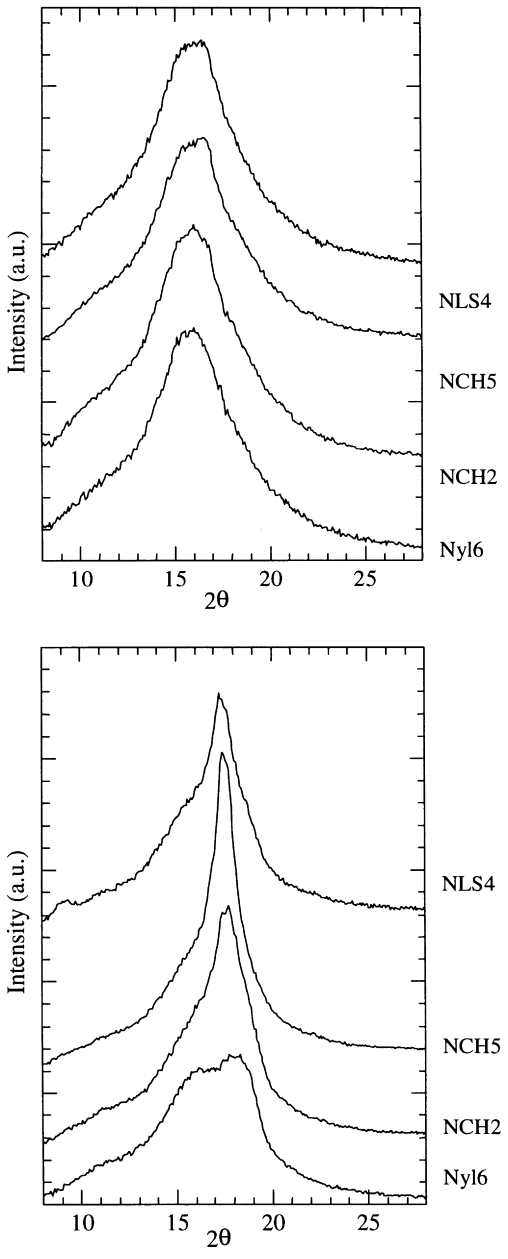

Fig. 7. WAXS profiles of nylon-6 and the PLSNs at 250 (melt) and 205°C. The curves are vertically offset for clarity.

markedly suppressed with a small volume fraction addition of montmorillonite. Disruption of the crystalline superstructure is anticipated to impact the fracture properties; however, the extent is yet to be determined.

These morphological features arise from the very inception of crystallization and finer details associated with silicate morphology and interfacial interactions are apparent at elevated temperatures. Results from the correlation function analysis of the excess scattering data at 205°C show that the long period, crystal lamella thickness, invariant, and the Porod constant all decrease for the end-tethered chains (NCH2 and NCH5) but increase for the melt-processed nanocomposite (NLS4). Decreases in the Porod constant and invariant typically denote a general decrease in lamellar ordering or decrease of scattering contrast between crystalline and amorphous polymer arising from incorporation of defects in the crystal phase. Tethering of the chains to the surface of the silicate layers reduces chain mobility and the potential orientation of crystallite near the silicate surface. Reduced mobility of the polymer chains will lead to smaller, less-ordered crystallites. For example, Charoensirisomboon et al. report disordered lamellae in polysulfone/nylon-6 blends as a consequence of polyamide chains attached to the surface of the polysulfone particles [25]. In contrast for NLS4, polymer chains weakly interacting with the silicate layer are not as impeded and are easier to incorporate into the crystal growth surface. The increased long spacing, crystal thickness, invariant, and Porod constant over the pure polymer indicate that in this case the layers aid superstructure formation of nylon-6 crystallites.

Results from analysis of the WAXS profiles indicate that the large interfacial area between the polymer and silicate effect the short-range order of the crystallites. In contrast to a silicate-independent amorphous chain–chain distance, a measurable shift in crystalline chain–chain distance is observed with addition of silicate. The larger inter-chain distances may indicate the formation of more defect-ridden crystallites due to poor incorporation of the chains into the lamellar structure because of hindered mobility associated with the layers. Despite the disorder of the lamellae and decreased crystallite size, the extent of crystallinity for a given isothermal anneal increases with addition of silicate, implying that the silicate layers act as nucleation agents and/or growth accelerators. Previously, unexfoliated organically modified montmorillonite has been shown to act as a nucleating agent in semicrystalline polymers [66]. Related

Table 2
WAXS results for pure nylon-6 and the nanocomposites in the molten (250°C) and semicrystalline (205°C) states (a) amorphous peak and (b) crystalline peak

	t_{cryst} (min)	2θ of amorphous peak ($\pm 0.1°$)	inter-chain spacing (± 0.03 Å)	ϕ_{mc} (%)
(a)				
250°C				
Nyl6		15.4	4.88	
NCH2		15.4	4.88	
NCH5		15.5	4.85	
NLS4		15.4	4.88	
205°C				
Nyl6		16.1	4.67	
NCH2		16.3	4.61	
NCH5		16.4	4.58	
NLS4		16.2	4.64	
(b)				
205°C				
Nyl6	85	17.9	4.20	7.3
NCH2	65	17.2	4.37	19.1
NCH5	65	17.0	4.42	22.4
NLS4	81	16.9	4.45	14.0

investigations in nylon-6 blends have shown a similar increase in crystallinity with an associated decrease in crystallite size [67]. Finally, the presence of the amide hydrogen-bond layer reflection ($2\theta = 8.6$) in NLS4 and absence in NCH2 and NCH5 at 205°C reinforces the supposition that end-tethering of the chains greatly reduces ability to be incorporated into a three-dimensional equilibrium crystal phase during the crystallization process. The development of the room-temperature phase and the kinetics of crystallization are currently under investigation.

6. Conclusions

Experimental results indicate that the development of polymer crystal morphology in semicrystalline layered silicate nanocomposites depends critically on the polymer/surface interactions as well as the organization of the silicate layers. SAXS revealed that long-range correlations occur in these nanocomposites at 40–60 nm, providing a confined environment for crystallization. Simultaneous SAXS and WAXS at elevated temperatures and correlation analysis of the scattering associated with the polymer crystallites provides detailed information on the influence of this mesoscale structure on the morphology of the polymer. The presence of these layers disrupts crystallite formation and results in less-ordered crystal phase, ultimately resulting in the predominance of the γ phase in quenched samples. Furthermore, the extent of interactions between the layer and polymer affect the crystallization process. Further examination of these effects will be reported shortly. These results indicate that it is critical to consider process-history and subsequent morphology of the crystal phase in semicrystalline polymer-nanocomposites, since the crystal phase will have a large impact on the final properties of the nanocomposite.

Acknowledgements

Partial funding was provided by the Air Force Office of Scientific Research and the Air Force Research Laboratory, materials and manufacturing Directorate. The authors would also like to acknowledge the help of F. Yeh (in situ SAXS and WAXS experiments at Brookhaven National Laboratory); and helpful discussions with R. Krishnamoorti and D. Hunter. The Advanced Polymers Beamline is supported by DOE (DE-FG02-99ER 45760) and the APPRT.

References

[1] Kojima Y, Usuki A, Kawasumi M, Okada O, Fukushima Y, Kurachi T, Kamigaito O. J Mater Res 1993;8:1185.
[2] Liu L, Qi Z, Zhu X. J Appl Polym Sci 1999;71:1133.
[3] Ke Y, Long C, Qi Z. J Appl Polym Sci 1999;71:1139.
[4] Messersmith PB, Giannelis EP. J Polym Sci, Part A: Polym Chem 1995;33:1047.
[5] Akelah A, Moet A. J Mater Sci 1996;31:3589.
[6] Kojima Y, Usuiki A, Kawasumi M, Okada A, Kurachi T, Kamigaito O. J Appl Polym Sci 1993;49:1259.
[7] Hseih D-T, Lloyd TB, Rutledge SK, Int. SAMPE Symp Proc, Conf Proc of 1998 meeting. (part 2 of 2) v 43 n2 SAMPE Covina, CA pp. 1170–1.
[8] Vaia RA, Price G, Ruth PN, Nguyen HT, Lichtenhan J. Appl Clay Sci 1999;15:67.
[9] Yano K, Usuki A, Kurachi T, Kamigaito O. J Polym Sci, Part A: Polym Chem 1993;31:2493.
[10] Kawasumi M, Hasegawa N, Kato M, Usuki A, Okada A. Macromolecules 1997;30:6333.
[11] Usuki A, Kojima Y, Kawasumi M, Okada A, Kukushima Y, Kurauchi T, Kamigaito O. J Mater Res 1993;8:1179.

[12] Fukushima Y, Inagaki S. J Inclusion Phenom 1987;5:473.
[13] Sikka M, Cerini LN, Ghosh SS, Winey KI. J Polym Sci, Part B: Polym Phys 1996;34:1443.
[14] Kurokawa Y, Yasuda H, Oya A. J Mater Sci Lett 1996;15:1481.
[15] Laus M, Francescangeli O, Sandrolini F. J Mater Res 1997;12:3134.
[16] Carrado KA, Xu L. Chem Mater 1998;10:1440.
[17] Kojima Y, Usuki A, Kawasumi M, Okada A, Kurachi T, Kamigaito O, Kaji K. J Polym Sci, Part B: Polym Phys 1995;33:1039.
[18] Kojima Y, Matsuoka T, Takahashi H, Kurachi T. J Appl Polym Sci 1994;51:683.
[19] Mathias LJ, Davis RD, Jarrett WL. Macromolecules 1999;32:7958.
[20] Ito M, Mizuochi K, Kanamoto T. Polymer 1998;39:4593.
[21] Jimenez G, Ogata N, Kawai H, Ogihara T. J Appl Polym Sci 1997;64:2211.
[22] Joanny J-F. Langmuir 1992;8:989.
[23] Semenov AN. Langmuir 1995;11:3560.
[24] Mansky P, Russell P, Hawker CJ, Pitsikalis M, Mays J. Macromolecules 1997;30:6810.
[25] Charoensirisomboon P, Saito H, Inoue T, Weber M, Koch E. Macromolecules 1998;31:4963.
[26] Krishnamoorti R, Giannelis EP. Macromolecules 1997;30:4097.
[27] Vaia RA, Jandt KD, Kramer EJ, Giannelis EP. Chem Mater 1996;8:2628.
[28] Vali H, Köster HM. Clay Miner 1986;21:827.
[29] Vali H, Hesse R. Am Miner 1990;75:1443.
[30] Marcks CH, Waschsmuth H, Reichenbach HGV. Clay Miner 1989;24:23.
[31] Klimentidis RE, Mackinnon IDR. Clays Clay Miner 1986;34:155.
[32] Hsiao BS, Gardner KH, Wu DQ, Chu B. Polymer 1988;29:1745.
[33] Rapp G, Gabriel A, Dosiere M, Kock MHJ. Nucl Inst Meth Phys Res A 1995;357:178.
[34] Verma R, Marand H, Hsiao BS. Macromolecules 1996;29:7767.
[35] Balta-Calleja FJ, Vonk GG. X-ray scattering of synthetic polymers. New York: Elsevier Science, 1989.
[36] Vonk CG, Kortleve G. Colloid Polym Sci 1967;220:19.
[37] Vonk CG. J Appl Cryst 1973;6:81.
[38] Ruland W. Colloid Polym Sci 1977;255:417.
[39] Stribeck N, Ruland W. J Appl Cryst 1978;11:535.
[40] Hsiao BS, Verma RK. J Synchrotron Rad 1998;5:23.
[41] Koberstein JT, Morra B, Stein RS. J Appl Cryst 1980;13:34.
[42] Glatter O. Small angle X-ray scattering. New York: Academic Press, 1982 (chap. IV, p. 167).
[43] Strobl GR, Schneider M. J Polym Sci, Polym Phys Ed 1980;18:1343.
[44] Murthy NS. Polym Comm 1991;32:301.
[45] Vaia RA, Giannelis EP. Macromolecules 1997;30:8000.
[46] Glatter O, Kratky O. Small angle X-ray scattering. New York: Academic Press, 1982.
[47] Vaia RA. In: Pinnavaia TJ, Beall G, editors. Polymer–clay nanocomposites, New York: Wiley, 2000.
[48] Morvan M, Espinat D, Lambard J, Zemb T. Colloids Surf. A: Physiochem Engng Asp 1994;82:193.
[49] Ginzburg VV, Balazs AC. Macromolecules 1999;32:5681.
[50] Lyatskaya Y, Balazs A. Macromolecules 1998;31:6676.
[51] Ginzburg VV, Balazs AC. Macromolecules 1999;32:5681.
[52] Pignon F, Magnin A, Piau JM, Cabane B, Linder P, Diat O. Phys Rev E 1997;56(3):3281.
[53] Pignon F, Piau JM, Magnin A. Phys Rev Lett 1996;76(25):4857.
[54] Pignon F, Magnin A, Piau JM. Phys Rev Lett 1997;79(23):4689.
[55] Hsiao BS, Wang Z, Yeh F, Yan G, Sheth KC. Polymer 1999;40:3515.
[56] Wang Z, Hsiao BS, Sauer BB, Kampert WG. Polymer 1999;40:4615.
[57] Wang Z, Hsiao BS, Murthy NS. J Appl Cryst 2000 (in press).
[58] Wallace WE, Beck Tan NC, Wu WL, Satija S. J Chem Phys 1998;108:3798.
[59] Forrest JA, Dalnoki-Veress K, Dutcher JR. Phys Rev E 1998;58:6109.
[60] Murthy NS, Curran SA, Aharoni SM, Minor H. Macromolecules 1991;24:3215.
[61] Vasanthan N, Murthy NS, Bray RG. Macromolecules 1998;31:8433.
[62] Parker JP, Lindenmeyer PH. J Appl Polym Sci 1977;21:821.
[63] Murthy NS, Aharoni SM, Szollosi AB. J Polym Sci: Polym Phys Ed 1985;23:2549.
[64] Keil W, Trafara G. Kautschuk + Gummi Kunststoffe 1993;46:105.
[65] Kyu T, Zhou L, Zhu C, Tajuddin Y, Qutubuddin S. J Polym Sci, Part B: Polym Phys 1996;34:1761.
[66] Mudra I, Balázs G. J Therm Anal 1998;52:355.
[67] Wang H-H, Chen W-L. J Polym Sci, Part A: Polym Chem 1990;28:2403.